11th International Symposium on Turbulence and Shear Flow Phenomena (TSFP11)
Southampton, UK, July 30 to August 2, 2019

VERY LARGE-SCALE MOTIONS IN VON KÁRMÁN FLOW

Pawel Baj [1]
pawel.baj@ntnu.no

James R. Dawson [1]
james.r.dawson@ntnu.no

Nicholas A. Worth [1]
nicholas.a.worth@ntnu.no

Anna N. Knutsen [1]
anna.n.knutsen@ntnu.no

John M. Lawson [2,3]
john.lawson@ds.mpg.de

Eberhard Bodenschatz [2]
eberhard.bodenschatz@ds.mpg.de

1: Department of Energy and Process Engineering
Norwegian University of Science and Technology
NO-7941 Trondheim, Norway

2: Laboratory for Fluid Physics, Pattern Formation and Biocomplexity
Max Planck Institute for Dynamics and Self-Organization
37077 Göttingen, Germany

3: Aerodynamics and Flight Mechanics Group
University of Southampton
Southampton SO171BJ, UK

ABSTRACT

The von Kármán swirling flow, produced by two counter-rotating disc in two different experimental facilities, is investigated experimentally by means of Stereoscopic and Scanning-volumetric Particle Image Velocimetry (PIV). A clear spectral peak is observed in Power Density Spectra (PSDs) of the velocity fluctuations in the vicinity of the flow's stagnation point near the centre of the tank. Its frequency is found to be lower by order of magnitude than the impeller frequency, indicative of a large-scale motion. Application of the conditional averaging and Proper Orthogonal Decomposition (POD) provides insight into the topology of the flow structure. We find that the structure can be described as an approximately unidirectional, radially-oriented velocity field which undergoes a slow precession around the tank's axis. This phenomenon appears to be persistent as it is detected in all the studied flow cases. An analysis of dynamics of the structures shows that it corresponds to the unstable eigenvalues of the linear term of the momentum equation, indicating what it is a global instability mode of a von Kármán flow.

INTRODUCTION

Very large-scale motions (VLSMs) are features observed in a wide range of turbulent flows, e.g. boundary layer flows, Rayleigh–Bernard cells or Taylor–Couette flows, but have yet to be observed in stationary turbulence produced in von Kármán type swirling flows. The latter has been used for turbulence research for almost a century (see e.g. Batchelor (1951), Mordant *et al.* (2004)) because it allows for measurements of high Reynolds numbers in a relatively small laboratory (see e.g. Rousset *et al.* (2014)). Von Kármán flows provide a reasonable experimental approximation of homogeneous isotropic turbulence state (HIT, see Debue *et al.* (2018)) due to its vanishing mean flow making it suitable for Lagrangian measurements with relatively long tracks (Ouellette *et al.* (2006)).

The current work investigates low-frequency dynamics associated with VLSM found in von Kármán flows. We report the existence of energetic, radially-oriented velocity structure present in the central region of the tank, which precesses around the tank's axis with a characteristic frequency an order of magnitude lower than the stirring frequency. This phenomenon appears persistently in five experimental datasets gathered in two different von Kármán tank facilities. We characterise the structure in terms of its energy content, topology, and its implications for meandering of the flow's stagnation point (see Worth (2010)). Recent studies have identified slow dynamics of a von Kármán swirling flow (e.g. De la Torre & Burguete (2007); López-Caballero & Burguete (2013)), mostly in a context of the mean flow's symmetry breaking. In particular, it has been observed that a frontier between two toroidal flow structures associated with particular impellers (see fig. 1 for a schematic of the flow) shifts from its initial central position

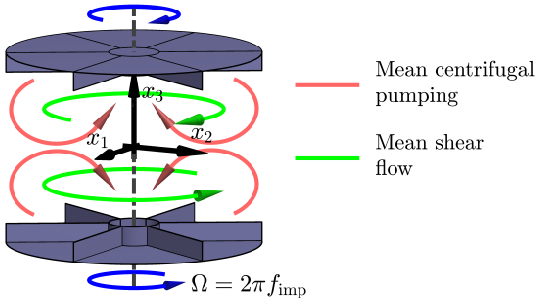

Figure 1: General schematic of a von Kármán flows studied.

Table 1: Parameters of setups (Δx, N, η stand respectively for the experiment's resolution, number of acquired snapshots and the Kolmogorov length-scale).

	Stereo PIV (GTF2)	Scanning PIV (GTF3)	Scanning PIV (BMT)
$1000 \cdot \mathrm{FoV}/R$	128×166	$34 \times 34 \times 34$	$161 \times 160 \times 33$
$\Delta x/\eta$	3.1	3.2	6.1
T_{acq} [s]	~ 2	~ 4	$90 <$
N	40000	200000	1000
f_{imp} [Hz]	$0.2 - 0.4$	0.2	0.0056
Re	$2 \times 10^4 - 4 \times 10^4$	2×10^4	2.3×10^4

towards one of the impellers as the Reynolds number exceeds a critical value, and, subsequently, it flips randomly from one side to the other with a time-scale much longer than the stirring time-scale. As a result, the flow's symmetry around the equator is lost. Such behaviour, however, is not observed in the present study. The topology of the reported structure resembles so-called macro-instabilities reported in stirred vessel flows (e.g. Doulgerakis *et al.* (2011)). The debate on the origins of those is still ongoing, and the present finding may bring a new perspective.

EXPERIMENTAL SETUP

Data gathered in two baffled von Kármán tank facilities is utilised in the preset study: the Cambridge Big Mixing Tank (BMT), and the Göttingen Turbulence Facility (GTF). These experimental rigs differ in terms of their design and have previously been comprehensively documented (Lawson & Dawson (2014), Xu *et al.* (2007)). We summarise the details of these facilities here only briefly. The GTF consisted of a steel cylinder (radius $R_{\mathrm{t}} = 24\,\mathrm{cm}$, height $H = 58\,\mathrm{cm}$), and two counter rotating impellers (radius $R = 12.5\,\mathrm{cm}$). Short, equidistant, axial baffles were attached to the cylinder's inside wall at the top and at the bottom (8 at each side), whilst the central area of the cylinder's inside wall remained unbaffled. The BMT is a dodecagonal tank (distance between its parallel walls $2R_{\mathrm{t}} = 2\,\mathrm{m}$, $H = 2\,\mathrm{m}$), with 12 axial baffles attached in corners of the inner walls of the tank, and two counter rotating impellers ($R = 0.8\,\mathrm{m}$). Figure 1 presents a schematic of the flow configuration and the coordinate used.

Stereoscopic and Scanning-volumetric Particle Image Velocimetry (abbreviated as Stereo PIV and Scanning PIV) techniques were employed (see Lawson & Dawson (2014)). The Stereo PIV measurements were performed only in GTF (labels GTF2 and GTF3 are used hereafter to designate respectively Stereo PIV, and Scanning PIV results obtained in the GTF facility). In each case, the field of view (FoV) was located in the vicinity of the tank's centre. Reynolds number Re based on the radius R and the impellers frequency f_{imp} (i.e. $Re = 2\pi R^2 f_{\mathrm{imp}}/\nu$, where ν stands for the kinematic viscosity) was equal to 2.3×10^4 and 2×10^4 for datasets BMT and GTF3. Three different Re values were tested within dataset GTF2: 2×10^4, 3×10^4, and 4×10^4. In all the experiments the acquisition period T_{acq} was comparable with the impellers' revolution period f_{imp}^{-1} (it was assumed that the fluctuations decorrelate with a substantially smaller time scale). In cases of Scanning PIV experiments, the acquisition consisted of short, time-resolved series of snapshots instead of just a single snapshot. This allowed us to resolve acceleration and pressure fields. The Stereo PIV data was processed using commercial PIV software (LaVision DaVis). The Scanning PIV data was processed using a dedicated in-house code. It returned velocity fields as well as associated acceleration and pressure fields. The divergence correction, as described by Wang *et al.* (2017), was applied to the resultant velocity field. Further details of setups are summarised in table 1.

As a final remark it should be noted, that these experiments were originally intended for the interrogation of small scales of turbulent motion, and thus their parameters are not optimised for large-scale measurements. However, in the course of these studies large scales features were discovered and are the focus of this paper.

RESULTS

As stated above, the experimental data was independently sampled assuming the largest time-scale was of order of the rotation speed f_{imp}^{-1}. However, an initial interrogation of temporal power spectral densities (PSDs) of velocity components presented in fig. 2 (for clarity, only results based on GTF3 are presented, PSDs in the remaining cases look alike) shows this is not the case. Firstly, the PSDs are not flat as they would be in the case of independent snapshots. Secondly, broad peaks appear in PSDs of velocity components perpendicular to the tank's axis (i.e. u_1, u_2). They occur at relatively low frequencies at an order of magnitude smaller than f_{imp}. This observation was found to be consistent across all our experiments. A mild decrease of the peaks' frequency is observed as the Reynolds number increases: from $0.126\,f_{\mathrm{imp}}$ at $Re = 2 \times 10^4$ to $0.116\,f_{\mathrm{imp}}$ at $Re = 4 \times 10^4$. It is noteworthy that López-Caballero & Burguete (2013) reported a spectral peak located roughly at $0.1\,f_{\mathrm{imp}}$ in a von Kármán swirling flow, however, it was only observed by the author in the vicinity of the side wall (their tank was unbaffled), and no peaks were observed around the tank's centre.

Although the spectral peaks depicted in fig. 2 are relatively modest in amplitude, their appearance suggests the existence of a large, slow-moving periodic or quasi-periodic structure in the flow. Insight into its topology can be gained through conditional averaging, based on a sufficient conditioning variable. Such a variable is not available to us *a priori*, but can be inferred from the velocity fluctuations. Towards this purpose, let us consider an instantaneous velocity field spatially-averaged over the FoV, designated as

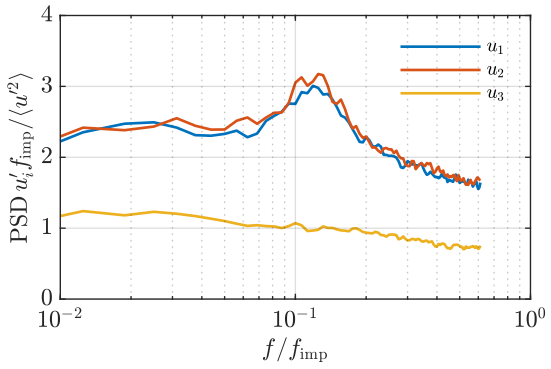

Figure 2: PSDs of particular components of the velocity field (based on GTF3).

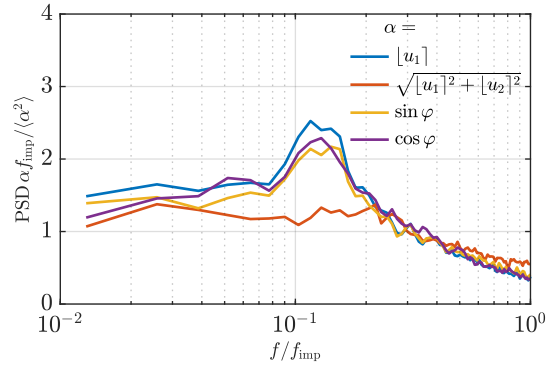

Figure 3: PSDs of u_1 and the factors of its decomposition: the magnitude direction and cosine (based on GTF2).

$\lfloor \boldsymbol{u} \rceil$. It was noticed, that in our considered case $\lfloor \boldsymbol{u} \rceil$ is coarsely representative of the entire instantaneous velocity field enclosed in the FoV, i.e. $\left(\lfloor \boldsymbol{u} \rceil\right)_{\mathrm{rms}} \simeq 0.77 u_{\mathrm{rms}}$ (based on the dataset GTF2). Moreover, the PSD of $\lfloor \boldsymbol{u} \rceil$ is very similar to that of $\boldsymbol{u}$ (as shown in fig. 3). Components of $\lfloor \boldsymbol{u} \rceil$, which are parallel to the radial plane $(x_1 - x_2)$, can be further represented respectively as $\sqrt{\lfloor u_1 \rceil^2 + \lfloor u_2 \rceil^2}\cos\varphi$ and $\sqrt{\lfloor u_1 \rceil^2 + \lfloor u_2 \rceil^2}\sin\varphi$, where $\tan\varphi = \lfloor u_2 \rceil / \lfloor u_1 \rceil$. Figure 3 also shows PSDs of particular factors of this representation: $\sqrt{\lfloor u_1 \rceil^2 + \lfloor u_2 \rceil^2}$ and $\cos\varphi$. It demonstrates that φ is the only source of spectral peaks, rather the magnitude $\sqrt{\lfloor u_1 \rceil^2 + \lfloor u_2 \rceil^2}$. Based on this it can be concluded, that the velocity structure, whose imprint is the spectral peak, undergoes quasi-periodic rotation in the radial plane $(x_1 - x_2)$ and φ can be used as the conditioning basis. We use the prefix "quasi" as the large width of the peak, and the relatively large amount of energy spread across the remaining frequencies suggests that this precession is irregular. This was confirmed in an inspection of the temporal evolution of φ (not presented here for brevity).

$$\breve{\boldsymbol{u}}^{\varphi} \simeq C u_{\mathrm{rms}} \begin{bmatrix} 1 - (\breve{x}_k/\ell_k)^2 \\ (\mu_{22}\breve{x}_2 + \mu_{23}\breve{x}_3)/R_{\mathrm{t}} \\ \mu_{32}\breve{x}_2/R_{\mathrm{t}} \end{bmatrix}^T \qquad (1)$$

Conditional averaging was executed by binning velocity snapshots into a number of bins, based on the instantaneous value of φ, and then averaging over those bins. Note, that conditional averaging based on φ of a structure which rotates around the tank's axis is somewhat equivalent to imaging the resultant conditional structure from different angles. Thus a 3D reconstruction of the structure's topology is possible even in the case of the stereoscopic data. Further, it is convenient to express results of the conditional averaging in a new coordinate system $(\breve{x}_1, \breve{x}_2, \breve{x}_3)$, which rotates along with the structure, and whose origin is located on the structure's revolution axis (quantities with a breve mark are expressed in this new system hereafter). Figures 4a and 4b present a representation of the 3D-reconstructed shape of the conditionally-averaged velocity field, denoted as $\breve{\boldsymbol{u}}^{\varphi}$. Its topology is similar across all experiments and can be described as an almost unidirectional advection along $\breve{x}_1$. Iso-surfaces of the energy of $\breve{\boldsymbol{u}}^{\varphi}$ resemble prolate spheroids stretched along the axial direction. Conditional streamlines form a diverging spiral in the plane $(\breve{x}_2 - \breve{x}_3)$, which is normal to the main velocity direction. Figures 4c to 4f show profiles of $\breve{\boldsymbol{u}}^{\varphi}$ for a more quantitative description. We find that all the profiles collapse well when normalised with r.m.s. velocity u_{rms}, and when the spatial coordinate is normalised with R_{t}. $\breve{\boldsymbol{u}}^{\varphi}$ can be well-fitted with an analytical approximation given by eq. (1), where $\breve{u}_1^{\varphi}$ is the dominant component. Length scales ℓ_1, ℓ_2, ℓ_3 are respectively equal

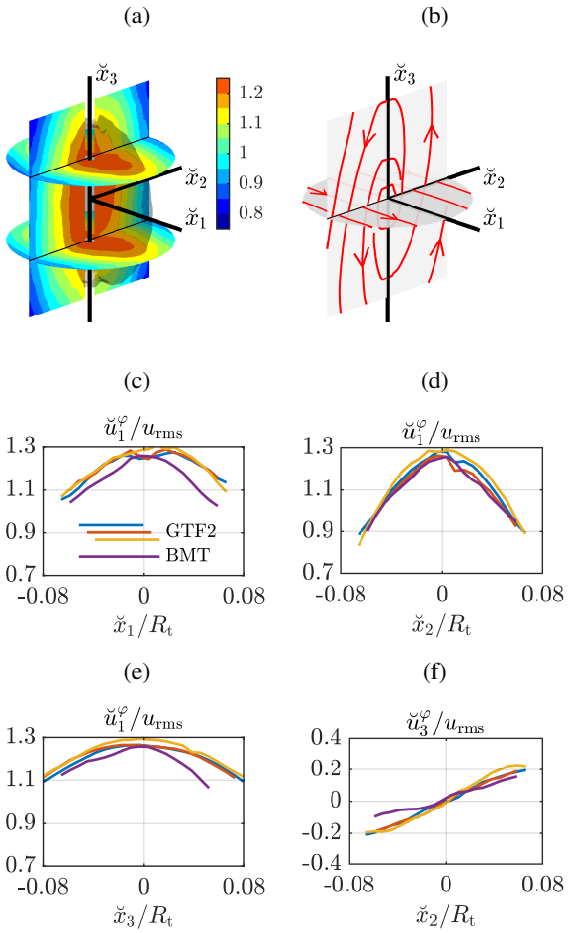

Figure 4: Conditionally-averaged velocity field $\breve{\boldsymbol{u}}^{\varphi}/u_{\mathrm{rms}}$: (a) slices through its magnitude (isosurface $|\breve{\boldsymbol{u}}^{\varphi}|/u_{\mathrm{rms}} = 1.15$ shown in gray), (b) 2-D streamlines ((a) – (b) based on GTF2), (c) – (f) profiles taken through the coordinate system origin.

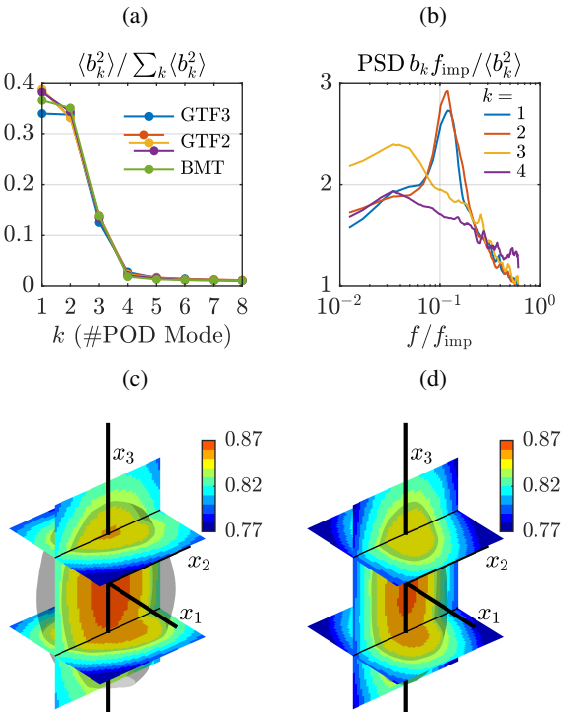

Figure 5: Results of POD: (a) energy distribution of the initial POD modes, (b) PSDs of the initial POD coefficients, (c) – (d) contribution to the velocity field (i.e. $|\boldsymbol{\Phi}^k b_k|/u_{\mathrm{rms}}$) from the first two POD modes (iso-surfaces $|\boldsymbol{\Phi}^k b_k|/u_{\mathrm{rms}} = 0.84$ shown in gray; (b)–(d) based on GTF3).

to $0.15R_\mathrm{t}$, $0.11R_\mathrm{t}$, $0.22R_\mathrm{t}$ (values averaged across all the datasets). If we define the size of the conditional structure as the spacing between the most distant zero-crossings of $\breve{u}_1^\varphi$, it equals $2\ell_3$ by extrapolation of eq. (1). Thus the structure occupies a large fraction of the total flow-fields; it is roughly two times larger than the integral length scale, which can be approximated as $0.18R_\mathrm{t}$ (when defined as an integral of the spatial correlation function of the velocity field). The scaling factor C is equal to 1.24, which implies that the contribution to the overall velocity fluctuation variance from the structure is dominant. Velocity component $\breve{u}_2^\varphi$ is the smallest, and thus not directly presented in fig. 4 for brevity. It can be fitted with the linear ansatz, where $\mu_{22} = 0.54$, and $\mu_{23} = -0.40$. $\breve{u}_3^\varphi$ is also roughly linear, with $\mu_{32} = 2.43$. The parameters μ_{ij} dictate the spiraling behaviour of the conditional streamlines in the plane $(\breve{x}_2 - \breve{x}_3)$.

We then applied a POD analysis to our datasets. In this framework a velocity field $\boldsymbol{u}$ is expressed as a superposition of the mean field $\bar{\boldsymbol{u}}$, and spatial POD modes $\boldsymbol{\Phi}_k$ multiplied by time-dependent coefficients b_k, as given by eq. (2) (N stands for the total number of modes). Figure 5a presents distributions of energy of the POD modes (i.e. $\overline{b_k^2}$), which overlap for all the datasets (for the purpose of this comparison FoVs were cropped to the same size before POD calculations; otherwise the distributions appear more scattered, although their qualitative nature is preserved). The majority of energy, over 65% of the total, is split evenly between the first two POD modes, while the remaining modes are much less energetic. Figure 5b shows PSDs of POD coefficients b_k. PSDs of the first two are very similar to those observed in PSDs of velocity fluctuations, which strongly suggests a link between the velocity spectral peaks and the

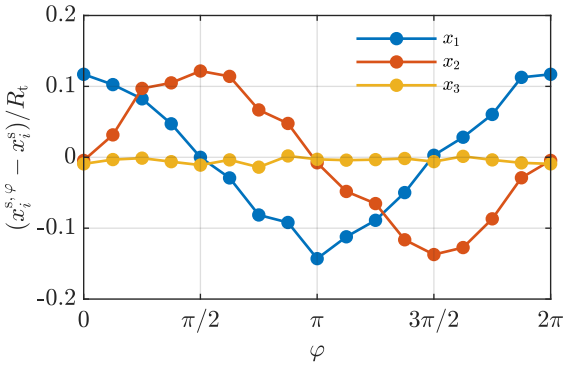

Figure 6: Relative coordinates of the conditionally-averaged stagnation point $\boldsymbol{x}^{\mathrm{s},\varphi}$ (based of GTF3).

first two POD modes. Figures 5c and 5d show the topology of the first two POD modes. They can be described as a unidirectional velocity field whose energy decay parabolically as moving away from the tank's centre. The appearance of modes 1 and 2 is similar, except for their different preferential directions, which are rotated by $\pi/2$ around the vertical axis (correlation between mode 1 and mode 2 after rotation by $\pi/2$ is of order 0.8, based on GTF3). The fact, that both the topology and magnitude of modes 1 and 2 are effectively the same, but phase-shifted by $\pi/2$, suggest that they are a single structure that rotates around the tank's axis. The velocity field spanned by these modes, i.e. $\boldsymbol{u}^{\mathrm{POD}} = \sum_{k=1}^{2} \boldsymbol{\Phi}^k b_k$, is very similar to the previously considered conditionally-averaged field, thus it can be concluded that both methods point to the same large-scale velocity structure.

$$\boldsymbol{u}(\boldsymbol{x},t) = \bar{\boldsymbol{u}}(\boldsymbol{x}) + \sum_{k=1}^{N} \boldsymbol{\Phi}^k(\boldsymbol{x}) b_k(t) \qquad (2)$$

A major implication of the appearance of the low-frequency instability is that it causes a meandering of the time-averaged flow's stagnation point $\boldsymbol{x}^{\mathrm{s}}$ around the tank's centre. Indeed, the position of the time-averaged flow's stagnation point is hard to converge as reported by Worth (2010) for example. To assess this effect, let us consider conditionally averaged coordinates of the stagnation point based on φ, denoted as $\boldsymbol{x}^{\mathrm{s},\varphi}$. The location of the conditional stagnation point as a function of φ, with respect to the averaged stagnation point, is presented in fig. 6. It is clear that it moves along a circular trajectory in the radial plane $(x_1 - x_2)$ as the velocity structure rotates. The exact value of the trajectory's radius, however, cannot be confidently inferred from the present experiment as it extends beyond of the FoV (values given in fig. 6 are based on an extrapolation of the velocity field of the dataset GTF3 under an assumption of constant velocity gradients). On the other hand, the axial coordinate $x_3^{\mathrm{s},\varphi}$ hardly change with φ and stays close to x_3^{s}. This is in agreement with previous observations of Worth (2010).

It is interesting to note that the revealed structure shares many similarities with macro-instabilities observed in stirred vessel flows (in such configurations there is a single impeller placed in the centre of the vessel). In particular, Doulgerakis *et al.* (2011) presented results of a POD analysis applied to planar PIV data; the FoV was parallel to the radial plane $(x_1 - x_2)$ and extended up to over $0.5R$. Simi-

lar to what is seen presently, the first two modes contained a roughly equal portion of the total energy. The characteristic frequency associated with these modes was approximated at $0.1 f_{\mathrm{imp}}$. The modes looked the same, except for the phase-shift of $\pi/2$. Close to the geometrical centre of the vessel, they generated a strong, locally unidirectional flow induced between a pair of counter-rotating axial vortices, located symmetrically around the centre line.

We now focus the dynamics of the considered velocity structure. Certain properties of POD make $\boldsymbol{u}^{\mathrm{POD}}$ better suited than $\breve{\boldsymbol{u}}^{\varphi}$ for this purpose (i.e. orthogonality of POD modes and POD coefficients), and thus $\boldsymbol{u}^{\mathrm{POD}}$ is used hereafter. The total velocity fluctuations $\boldsymbol{u}'$ can be decomposed into a contribution from the structure $\tilde{\boldsymbol{u}} = \boldsymbol{u}^{\mathrm{POD}}$, and residual fluctuations $\boldsymbol{u}'' = \boldsymbol{u}' - \tilde{\boldsymbol{u}} = \sum_{k=3}^{N} \boldsymbol{\Phi}^k b_k$. We establish the dynamical equation governing $\tilde{\boldsymbol{u}}$, by subtracting the time-averaged momentum equation from the momentum equation. By projecting the result onto $\boldsymbol{\Phi}^k$ (i.e. by evaluating $\int_{\mathrm{FoV}} \boldsymbol{\Phi}^k \cdot \frac{\partial}{\partial t}\boldsymbol{u}' \,\mathrm{d}\boldsymbol{x}$), one gets an ordinary differential equation (ODE), which dictates the evolution of the associated POD weightings b_k. Eventually, the first two ODEs are multiplied by the respective modes $\boldsymbol{\Phi}^k$, and summed together, yielding eq. (3), i.e. the dynamical equation governing $\tilde{\boldsymbol{u}}$ (the notation $\{\boldsymbol{\alpha}\}^k$ expands as $\int_{\mathrm{FoV}} \boldsymbol{\Phi}^k \cdot \boldsymbol{\alpha} \,\mathrm{d}\boldsymbol{x}$).

$$
\begin{aligned}
\frac{\partial \tilde{\boldsymbol{u}}}{\partial t} &= \sum_{k=1}^{2} \boldsymbol{\Phi}^k \frac{\partial b_k}{\partial t} \\
&= \sum_{k=1}^{2} \boldsymbol{\Phi}^k (C^k + L^{km} b_m + Q^{kmn} b_m b_n + \xi^k), \\
C^k &= \left\{ \frac{\partial \overline{u_i' u_j'}}{\partial x_i} \right\}^k, \quad Q^{kmn} = \left\{ \frac{\partial \Phi_i^m \Phi_j^n}{\partial x_i} \right\}^k, \\
L^{km} &= \left\{ \nu \frac{\partial^2 \Phi_j^m}{\partial x_i^2} - \frac{\partial}{\partial x_i} (\bar{u}_i \Phi_j^m + \Phi_i^m \bar{u}_j) \right\}^k, \\
\xi^k &= \left\{ \nu \frac{\partial^2 u_j''}{\partial x_i^2} - \frac{\partial}{\partial x_i} \left(u_i'' u_j + (\bar{u}_i + \tilde{u}_i) u_j'' \right) - \frac{\partial p'}{\partial x_j} \right\}^k
\end{aligned}
\tag{3}
$$

There are four main terms in eq. (3), which relate to their order in b_k. The constant term $\boldsymbol{\Phi}^k C^k$ represents the contribution from Reynolds stresses. The linear term $\boldsymbol{\Phi}^k L^{km} b_m$ corresponds to the interaction between $\bar{\boldsymbol{u}}$ and $\tilde{\boldsymbol{u}}$, and the viscous diffusion associated with $\tilde{\boldsymbol{u}}$. The quadratic term $\boldsymbol{\Phi}^k Q^{kmn} b_m b_n$ is the manifestation of the triple-correlation of components of $\tilde{\boldsymbol{u}}$. Finally, the high-order term $\boldsymbol{\Phi}^k \xi^k$ is dominated by self-interactions of $\boldsymbol{u}''$, as well as with $\tilde{\boldsymbol{u}}$ and the pressure field. Figure 7a shows rms fluctuations of radial components of these terms. Results obtained from datasets GTF3 and BMT are similar (although one should bear in mind the difference in the convergence of statistics evaluated from these two datasets, see table 1). Thus it can be reasonably argued, that this result is a robust representation of dynamics of the flow close to the centre of a von Kármán swirling flow. The high-order term $\boldsymbol{\Phi}^k \xi^k$ is the dominant one; it exceeds the linear term (which is the second most prominent) by almost an order of magnitude, while the remaining two terms are even smaller. Further insight into the dynamics of $\tilde{\boldsymbol{u}}$ is gained by examination of autocorrelation functions (ACFs) and PSDs of terms of eq. (3), depicted in figs. 7a and 7b (ACFs were averaged over all three velocity components). There is a clear, long-timescale oscillation of the ACF of the linear term (the period of the order of $8 f_{\mathrm{imp}}^{-1}$); the ACF is equal to 15% after

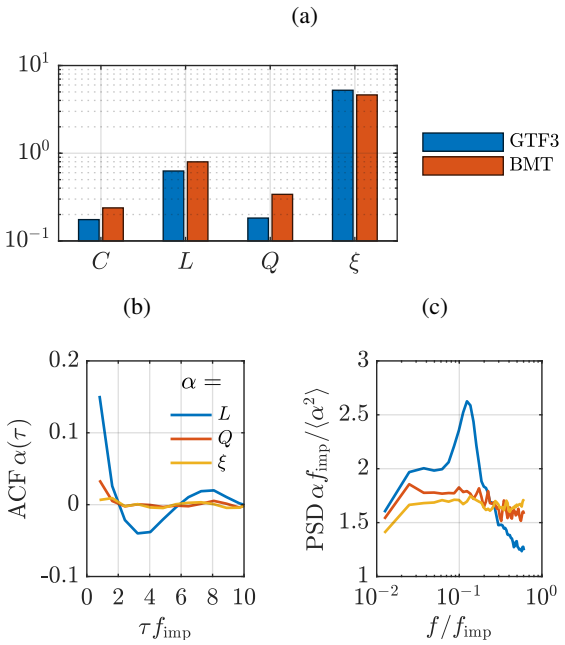

Figure 7: Fluctuations of radial components of terms of eq. (3): (a) levels of rms (normalised with $2\pi R f_{\mathrm{imp}}^2$, (b) ACFs, and (c) PSDs ((b) – (c) based on GTF3).

a single impeller revolution. On the other hand, ACFs of the remaining terms are flat and closely zero. Counterpart observations follow from PSDs. The spectrum of the linear term comprises a clear peak, whose locations correspond with those seen in fig. 2. PSDs of the remaining terms are almost precisely flat.

Based on the above analysis, the linear term of eq. (3) appears to drive the velocity structure recognised earlier, as only this term exhibits a peak in its PSD. The term's spectral properties are governed by eigenvalues of L^{km} (a matrix of the size 2×2), denoted here as ζ_L. In cases of both volumetric datasets, GTF3 and BMT, L^{km} is characterised by a pair of unstable eigenvalues, equal respectively to $0.30 \pm \mathrm{i}0.08$ and $0.37 \pm \mathrm{i}0.11$ (when normalised with $2\pi f_{\mathrm{imp}}$), which are similar results. It follows that the linear term of eq. (3) excites a certain structure (as $\Re(\zeta_L) > 0$), whose characteristic normalised frequency equals $\Im(\zeta_L)/2\pi f_{\mathrm{imp}}$. This coincides almost exactly with the characteristic frequency seen in fig. 2. The results strongly suggest, that the observed structure is a global instability mode (i.e. the unstable eigenmode of the linear term of the momentum equation). However, since the linear term constitutes a relatively small contribution to the total value of $\partial\tilde{\boldsymbol{u}}/\partial t$, the structure's oscillatory evolution enforced by this term can be intensively disturbed by more prominent terms. This correlates with the reported irregular precession of the structure, as well as with relatively broad support of the spectral peak seen in fig. 2.

Finally, let us consider sensitivity of eigenvalues of L^{km} to some basic parameters of the flow. It follows from eq. (3), that L^{km} is the function of a few parameters only: $\boldsymbol{\Phi}^k$, $\bar{\boldsymbol{u}}$, and ν (or equivalently Re). POD modes can be further approximated by eq. (1), which is dependant on a few scalar parameters. On the other hand, $\bar{\boldsymbol{u}}$ can be roughly approximated around the mean stagnation point $\boldsymbol{x}^{\mathrm{s}}$ with a linear function $\bar{u}_i \simeq \lfloor A_{ij} \rceil (x_j - x_j^{\mathrm{s}})$, where A_{ij} is the mean velocity gradient tensor (error of this approximation does not exceed 5% for the dataset GTF3, which is used in this analysis). The direct

sensitivity analysis to all these parameters can be performed once these approximations are substituted into the formula defining L^{km}. It has been found that the $\Re(\zeta_L)$, which relates to the mode's growth rate, is affected mostly by the diagonal elements of $\lfloor A_{ij} \rceil$ (i.e. $\partial\Re(\zeta_L)/\partial\lfloor A_{11}\rceil = 1.26$), and partially by Re (i.e. $\frac{Re}{2\pi f_{\text{imp}}}\partial\Re(\zeta_L)/\partial Re$=0.06). On the other hand, $\Im(\zeta_L)$, i.e. the normalised characteristic frequency of the mode, is dependent almost exclusively on $\lfloor A_{12}\rceil$ and $\lfloor A_{21}\rceil$ (i.e. $\partial\Im(\zeta_L)/\partial\lfloor A_{21}\rceil = 0.87$). Effects of the remaining parameters were found to be negligible.

SUMMARY & CONCLUSIONS

We analysed a von Kármán swirling flow near the tank's centre, based on a collection of experimental datasets across two different facilities. Basic characterisation of the velocity fields revealed the existence of a low-frequency large-scale motion whose time-scale is roughly $0.1 f_{\text{imp}}$ in all datasets. It is the dominant flow feature around the tank's centre, where homogeneous turbulence is produced, as it involves over 65% of the total flow's energy. This is very different from the homogeneous isotropic turbulence, which is characterised by more even energy distribution (von Kármán swirling flow is often compared with the latter due to the vanishing mean flow and homogeneous velocity fluctuations near the tank's centre, see e.g. Lawson & Dawson (2015)). We were able to extract the associated velocity structure utilising conditional averaging and POD (the first two POD modes represent the structure). A similar structure topology emerged from all the considered datasets, suggesting the robust nature of our finding. The structure can be briefly described as an almost unidirectional, radially-oriented velocity field, whose magnitude decreases parabolically as moving away from the tank's centre. It undergoes a slow, highly perturbed precession around the tank's axis. The approximated size of the structure equals roughly $0.45R_{\text{t}}$ (when sized based on the results of conditional averaging), which is over two times than the integral length scale. Thus the structure can be referred to as a (very) large-scale motion.

Analysis of the derived dynamical equation governing the evolution of the structure shows that its linear term is characterised by a pair of unstable eigenvalues. Their characteristic frequencies overlap with the peak frequency seen in the PSD of the velocity fluctuations. This indicates that the structure is a global instability of a von Kármán swirling flow. Although the linear term of eq. (3) is non-negligible, it is not the dominant one. Non-linear interactions involving the residual fluctuations are far more prominent by almost an order of magnitude. However, unlike the linear term, they lack a long-time correlation. These non-linear interactions can potentially disturb the periodic evolution of the structure driven by the linear term, which would explain the observed irregular structure's precession. A simple sensitivity analysis shows that the characteristic frequency depends mostly on two components of the velocity gradient tensor, i.e. A_{12} and A_{21}. It would be interesting to validate this observation in future research through altering non-dimensional values of A_{12} and A_{21}, possibly by varying design of baffles or by using a different aspect ratio of the tank.

The observed phenomenon is in many aspects similar to the so-called macro-instability reported in the context of stirred vessels (see e.g. Doulgerakis *et al.* (2011)). The origins of those macro-instabilities are debated in the scientific community. We believe that the present work, although not directly related to a stirred vessel flows, brings a valuable contribution to this debate. macro-instabilities are debated in the scientific community.

REFERENCES

Batchelor, G. K. 1951 Note on a class of solutions of the Navier-Stokes equations representing steady rotationally-symmetric flow. *Quart. J. Mech. Appl. Math.* **4** (1), 29–41.

Debue, P., Kuzzay, D., Saw, E.-W., Daviaud, F., Dubrulle, B., Canet, L., Rossetto, V. & Wschebor, N. 2018 Experimental test of the crossover between the inertial and the dissipative range in a turbulent swirling flow. *Physical Review Fluids* **3** (2), 024602.

Doulgerakis, Z., Yianneskis, M. & Ducci, A. 2011 On the manifestation and nature of macroinstabilities in stirred vessels. *AlChE J.* **57** (11), 2941–2954.

Lawson, J. M. & Dawson, J. R. 2014 A Scanning PIV method for fine-scale turbulence measurements. *Exp. Fluids* **55** (12), 1857.

Lawson, J. M. & Dawson, J. R. 2015 On velocity gradient dynamics and turbulent structure. *J. Fluid Mech.* **780**, 60–98.

López-Caballero, M. & Burguete, J. 2013 Inverse cascades sustained by the transfer rate of angular momentum in a 3D turbulent flow. *Physical review letters* **110** (12), 124501.

Mordant, N., Lévêque, E. & Pinton, J. F. 2004 Experimental and numerical study of the lagrangian dynamics of high Reynolds turbulence. *New J. Phys.* **6** (1), 116.

Ouellette, N. T., Xu, H., Bourgoin, M. & Bodenschatz, E. 2006 An experimental study of turbulent relative dispersion models. *New Journal of Physics* **8** (6), 109.

Rousset, B., Bonnay, P., Diribarne, P., Girard, A., Poncet, J.-M., Herbert, E., Salort, J., Baudet, C., Castaing, B., Chevillard, L. *et al.* 2014 Superfluid high Reynolds von Kármán experiment. *Rev. Sci. Instrum.* **85** (10), 103908.

De la Torre, A. & Burguete, J. 2007 Slow dynamics in a turbulent von Kármán swirling flow. *Physical review letters* **99** (5), 054101.

Wang, C., Gao, Q., Wei, R., Li, T. & Wang, J. 2017 Weighted divergence correction scheme and its fast implementation. *Exp. Fluids* **58** (5), 44.

Worth, N. A. 2010 Tomographic PIV measurement of coherent dissipation scale structures. PhD thesis, University of Cambridge.

Xu, H., Ouellette, N. T., Vincenzi, D. & Bodenschatz, E. 2007 Acceleration correlations and pressure structure functions in high-Reynolds number turbulence. *Physical review letters* **99** (20), 204501.